**UDC** 669.245.018.44: 091.3-977

**DOI** dx.doi.org/10.17073/1997-308X-2022-3-4-23

### Oxidation kinetics and mechanism of nickel alloys

© 2022 г. M.I. Aheiev, V.V. Sanin, N.V. Shvindina, Yu.Yu. Kaplanskii, E.A. Levashov

National University of Science and Technology (NUST) «MISIS», Moscow, Russia

Received 16.03.2022, revised 21.03.2022, accepted for publication 01.04.2022

Abstract: The study covers the effect of alloying elements on the kinetics and mechanism of oxidation at 1150 °C for 30 hours of heat-resistant nickel alloys obtained using such technologies as centrifugal SHS metallurgy (SHS(M)), vacuum induction melting (VIM), elemental synthesis (ES), hot isostatic pressing (HIP). A comparative analysis was carried out for alloys based on nickel monoaluminide and standard AZhK and EP741NP alloys. It was found that kinetic dependences are described mainly by parabolic approximation. The logarithmic law of oxidation with the rapid (within 3-4 hours) formation of the primary protective layer is typical for alloys doped with molybdenum and hafnium. In the case of AZhK and EP741NP, oxidation proceeds according to a parabolic law at the initial stage (2-3 hours), and then according to a linear mechanism with the voloxidation and complete destruction of samples. Oxygen and nitrogen diffusion proceeds predominantly along the nickel aluminide grain boundaries and it is limited by the  $Al_2O_3 + Cr_2O_3 + X_nO_m$  protective film formation. SHS(M) alloys feature by a positive effect of zirconium and tantalum added as dopants on heat resistance. The Ta<sub>2</sub>O<sub>5</sub> phase is formed in the intergranular space, which reduces the rate and depth of oxidation. The zirconium-containing top layer  $Al_2O_3 + Zr_5Al_3O_{0.5}$  blocks the external diffusion of oxygen and nitrogen, thereby improving heat resistance. Doping with hafnium also has a positive effect on oxidation resistance and leads to the formation of submicron and nanosized HfO<sub>2</sub> inclusions that suppress the grain boundary diffusion of oxygen. Mo<sub>3</sub>O<sub>4</sub>, CoMoO<sub>4</sub> volatile oxides are formed in alloys with a high content of molybdenum and compromise the protective layer integrity. A comparative analysis of the oxidation kinetics and mechanism for samples consisting of the base  $\beta$ -alloy with Cr + Co + Hf additives showed a significant effect on the heat resistance of the sample preparation method. As the proportion of impurity nitrogen decreases and the Cr<sub>2</sub>O<sub>3</sub> sublayer is formed, the oxidation mechanism also changes.

Keywords: nickel alloys, heat resistance, oxidized layer, centrifugal SHS metallurgy, elemental synthesis.

**Aheiev M.I.** – Junior research scientist, Scientific-Educational Center of SHS, National University of Science and Technology (NUST) «MISIS» (119049, Russia, Moscow, Leninskiy pr., 4). E-mail: aheievmi@gmail.com.

**Sanin V.V.** – Cand. Sci. (Eng.), Junior research scientist, Scientific-Educational Center of SHS, MISIS-ISMAN. E-mail: sanin@misis.ru.

**Shvindina N.V.** – Scientific project engineer 1st category, Scientific-Educational Center of SHS, MISIS-ISMAN. E-mail: natali19-03@list.ru.

**Kaplanskii Yu.Yu.** – Cand. Sci. (Eng.), Research scientist, Scientific-Educational Center of SHS, MISIS-ISMAN. E-mail: ykaplanscky@mail.ru.

**Levashov E.A.** – Dr. Sci. (Eng.), Prof., Acad. of Russian Academy of Natural Science, Head of Scientific-Educational Center of SHS, MISIS–ISMAN; Head of the Department of powder metallurgy and functional coating, NUST «MISIS». F-mail: levashov@shs misis ru

**For citation:** Aheiev M.I., Sanin V.V., Shvindina N.V., Kaplanskii Yu.Yu., Levashov E.A. Oxidation kinetics and mechanism of nickel alloys. *Izvestiya Vuzov. Poroshkovaya Metallurgiya i Funktsional'nye Pokrytiya (Powder Metallurgy and Functional Coatings)*. 2022. Vol. 16. No. 3. P. 4–23 (In Russ.). DOI: dx.doi.org/10.17073/1997-308X-2022-3-4-23.

#### Кинетика и механизм окисления никелевых сплавов

М.И. Агеев, В.В. Санин, Н.В. Швындина, Ю.Ю. Капланский, Е.А. Левашов

Национальный исследовательский технологический университет (НИТУ) «МИСиС», г. Москва, Россия

Статья поступила в редакцию 16.03.2022 г., доработана 21.03.2022 г., подписана в печать 01.04.2022 г.

**Аннотация:** Исследовано влияние легирующих элементов на кинетику и механизм окисления при температуре 1150 °C в течение 30 ч жаропрочных никелевых сплавов, полученных по технологиям центробежной СВС-металлургии (СВС-М),

вакуумного индукционного переплава (ВИП), элементного синтеза (ЭС) и горячего изостатического прессования (ГИП). Проведен сравнительный анализ сплавов на основе моноалюминида никеля и стандартных сплавов марок АЖК и ЭП741НП. Выявлено, что кинетические зависимости описываются преимущественно параболической аппроксимацией. Логарифмический закон окисления с быстрым (в течение 3-4 ч) формированием первичного защитного слоя характерен для сплавов, легированных молибденом и гафнием. В случае АЖК и ЭП741НП на начальной стадии (2-3 ч) окисление происходит по параболическому закону, а в дальнейшем - по линейному механизму с объемным окислением и полным разрушением образцов. Диффузия кислорода и азота протекает преимущественно по границам зерен алюминида никеля и лимитируется образованием защитной пленки состава  $Al_2O_3 + Cr_2O_3 + X_nO_m$ . Для сплавов, полученных методом СВС-М, характерным является положительное влияние на жаростойкость легирующих добавок циркония и тантала. В межзеренном пространстве образуется фаза Та<sub>2</sub>О<sub>5</sub>, которая снижает скорость и глубину окисления. Цирконийсодержащий верхний слой  $Al_2O_3 + Zr_5Al_3O_{0.5}$  блокирует внешнюю диффузию кислорода и азота, тем самым повышая жаростойкость. Легирование гафнием также положительно сказывается на окислительной стойкости сплавов и приводит к образованию субмикронных и наноразмерных включений HfO2, которые подавляют зернограничную диффузию кислорода. В образцах с повышенным содержанием молибдена формируются летучие оксиды  $MoO_3$ ,  $Mo_3O_4$ ,  $CoMoO_4$ , которые разрушают целостность защитного слоя. Сравнительный анализ кинетики и механизма окисления образцов из базового β-сплава с добавками Cr + Co + Hf показал существенное влияние на жаростойкость способа получения образцов. При снижении доли примесного азота и образования подслоя Cr<sub>2</sub>O<sub>3</sub> меняется и механизм окисления.

*Ключевые слова:* никелевые сплавы, жаростойкость, окисленный слой, центробежная СВС-металлургия, элементный синтез.

**Агеев М.И.** – мл. науч. сотрудник Научно-учебного центра (НУЦ) СВС, МИСиС-ИСМАН, НИТУ «МИСиС» (119049, г. Москва, Ленинский пр-т, 4). E-mail: aheievmi@gmail.com.

Санин В.В. - канд. техн. наук, мл. науч. сотрудник НУЦ СВС, МИСиС-ИСМАН. E-mail: sanin@misis.ru.

**Швындина Н.В.** – инженер научного проекта 1-й категории, НУЦ СВС, МИСиС-ИСМАН. E-mail: natali19-03@list.ru.

**Капланский Ю.Ю.** – канд. техн. наук, науч. сотрудник НУЦ СВС, МИСиС-ИСМАН. E-mail: ykaplanscky@mail.ru.

**Левашов Е.А.** – докт. техн. наук, акад. РАЕН, проф., директор НУЦ СВС, МИСиС-ИСМАН; зав. кафедрой порошковой металлургии и функциональных покрытий, НИТУ «МИСиС». E-mail: levashov@shs.misis.ru.

**Для цитирования:** *Агеев М.И., Санин В.В., Швындина Н.В., Капланский Ю.Ю., Левашов Е.А.* Кинетика и механизм окисления никелевых сплавов. *Известия вузов. Порошковая металлургия и функциональные покрытия.* 2022. Т. 16. No. 3. C. 4–23. DOI: dx.doi.org/10.17073/1997-308X-2022-3-4-23.

### Introduction

Alloys based on monoaluminide nickel are promising for using in components of gas-turbine engines. At the same time, they have low strength properties at room temperature, resulting in the high risk of fracture and insufficient processability due to difficult machining [1-5]. Plasticizing additives of chromium, molybdenum, and rare-earth elements are introduced into such materials, in order to increase fracture toughness [3—7]. In the case of hot-path alloys the key parameter is oxidation resistance at increased temperatures, fatigue and thermo-cycle impacts, as well as the degree of alloying and the surface state determine their heat resistance [8]. High-temperature oxidation as a type of chemical corrosion leads to an emergence of additional stress concentrators and reduction of mechanical properties due to softening of grain interfaces [8—14].

A comparison of thermodynamic calculations and experimental data regarding the oxidation process for coarse-grained nickel monoaluminide alloyed with chromium and molybdenum showed that oxides  $Cr_2O_3$  and  $Al_2O_3$  form a protective layer at the interfaces preventing oxygen diffusion. Molybdenum promotes formation of volatile suboxides which leave pores in the sample upon evaporation [15]. The formation of oxidized layers near the surface is selective in nature and depends on the composition of introduction elements in the  $\beta$ -phase, the temperature, and the oxidation environment [16].

Hierarchically structured  $\beta$ -alloys doped with chromium, cobalt and other elements with high heat resistance and creep resistance are known. Studies [17—25] show the possibility of obtaining spherical powders for

selective laser melting (SLM) by two process flowcharts: (1) centrifugal SHS casting (SHS-M), vacuum induction remelting (VIR), and plasma rotating electrode process; (2) elementary synthesis of powders (ES) and their plasma spheroidization. Authors [26] investigated the effect of an alloving element (X) on the resistance to elastic, plastic deformation and the creep activation energy (Q). Alloying enabled modification of the structure near the grain boundaries and binding of introduction elements in additional compounds. For example: molybdenum provided an increase in strength, thermal stability, creep resistance and resistance to sulfide corrosion. Zirconium reduced the size of structural components and increased the heat resistance. Introduction of tantalum marked an increase in creep resistance and fatigue strength of the alloy. Micro additions of rhenium during combined alloying with molybdenum in combination with heat treatment significantly increased the yield strength ( $\sigma_{vs}$ ), ultimate compressive strength ( $\sigma_{ucs}$ ) and the degree of plastic deformation (ε) [26]. Moreover, introduction of up to 15 % Mo and 1.5 % Re by the set of properties provided the greatest increase in mechanical properties of cast alloys [26].

When inheriting a 3-level structure of β-alloy doped with chromium, cobalt and hafnium, the evolution of its structure at all stages of production was noted: ES, hot isostatic pressing (HIP), SLM, SLM + HIP + heat treatment (HT) [27]. Precipitation tests of alloys in the temperature range of 600-1100 °C confirmed the necessity of after-treatment (HIP and HT) [27]. The simultaneous release of strengthening nanoparticles of the Laves phase (Cr<sub>2</sub>Nb, Co<sub>2</sub>Nb), Heusler phase (Ni<sub>2</sub>AlHf) and carbides (Hf<sub>x</sub>Nb<sub>v</sub>)C noticeably improved the mechanical properties of the alloy with niobium and hafnium. Alloying with chromium, cobalt and hafnium in the SLM + HIP +HT state at room temperature enabled the following level of properties to be obtained:  $\sigma_{ucs}$  = 2850 MPa,  $\sigma_{ys}$  = 1170 MPa,  $\epsilon$  = 16 %, and at t = 900 °C  $-\sigma_{ucs} = 378$  MPa,  $\sigma_{ys} = 300$  MPa, Q = 380 kJ/mol. The alloy with 0.9 % Hf surpassed the alloy with Cr, Co and 0.25 % Hf in terms of high-temperature strength and creep resistance at t = 900 °C:  $\sigma_{\text{ucs}} = 640 \text{ MPa}, \, \sigma_{\text{vs}} = 495 \text{ MPa}, \, Q = 775 \text{ kJ/mol}. \text{ It pos-}$ sessed close values of  $\sigma_{ucs} = 2720 \text{ MPa}$ ,  $\sigma_{vs} = 1220 \text{ MPa}$ , and  $\varepsilon = 12 \%$  at room temperature [27].

At the same time the question of the influence of the composition and method of production of nickel alloys on the oxidation resistance at high temperatures remains open. Therefore, the objective of the study was to compare the kinetics and mechanism of oxidation at t = 1150 °C for 30 h of nickel  $\beta$ -alloys, AZhK, EP741NP in the SHS-M, VIR, ES, HIP and HT states.

# Research materials and methods

In order to study heat resistance, samples were manufactured according to two process flowcharts (see the table): (1) centrifugal SHS casting by the method [18—20, 26], vacuum-induction remelting; (2) elementary synthesis of powder + hot isostatic pressing [28].

A well-known alloy [18, 25] with additions of chromium, cobalt and element (X) according to the table was chosen as the basis. For the base alloy represented by samples 8, 9 and 12, the dependences of heat resistance on the method of their production were plotted. The SHS-M alloys produced by centrifugal SHS casting were ingots with a diameter of 80 mm and height of 25-30 mm. They were obtained at an optimum centrifugal acceleration of  $a = 150\pm 5$  m/s<sup>2</sup> [26]. The features of synthesis are described in detail in [17, 18].

The ES method in the layer-by-layer burning mode was used to obtain sintered masses of 5 compositions (see the table). They were ground to a fraction of not less than 100 μm, after which the powder was consolidated by HIP on a gasostat HIRP10/26-200 (ABRA AG, Switzerland) according to [27]. The ES + HIP method is described in [22–25].

Samples 8 mm in diameter and 4 mm high were cut on an EDM machine GX-320L (CHMER EDM, China) and ground to a roughness of  $R_z = 5$ . Oxidative annealing was carried out in air at 1150 °C for 30 h with periodic weighing of the samples. The change in their mass, reduced to a unit surface area, over a certain period of time was evaluated. Based on the experimental data, oxidation curves were plotted and approximation equations were derived.

The phase composition of oxidation products was determined using *X*-ray diffraction phase analysis (XRD) on a diffractometer D2 PHASER (Bruker AXS GmbH, Germany) using  $CuK_{\alpha}$ -radiation in the range of angles of  $2\theta = 10^{\circ} \div 140^{\circ}$ .

The surface morphology and the interface of oxidized samples were studied using a scanning electron

## Content of alloying elements (X) and approximation equations for the oxidation function of the investigated $\boldsymbol{\beta}$ alloys

Содержание легирующих элементов (X) и уравнения аппроксимации функции окисления исследуемых β-сплавов

Sample No.	Method of production	Alloy element (X)	X, % wt./at.		Oxidation equation		
1		La	La	0.0831 / 0.03	$y = -0.0502x^2 + 3.1978x + 2.6451$		
2		Мо	Мо	2.44 / 1.18	$y = -0.0538x^2 + 3.2244x + 4.2907$		
3	SHS-M	Zr	Zr	0.48 / 0.24	$y = -0.0204x^2 + 1.2605x + 1.7022$		
4		Ta	Ta	2.11 / 1.07	$y = -0.028x^2 + 1.8015x + 2.9724$		
5		Re	Re	1.48 / 0.75	$y = -0.0469x^2 + 2.7109x + 4.0148$		
6		Мо	Мо	15.20 / 7.84	$y = 21.4\ln(x) + 31.7$		
7		Mo, Re	Мо	15.40 / 8.0	$y = 11.5\ln(x) + 41.7$		
7			Re	1.40 / 0.40			
8		Hf	Hf	0.98 / 0.25	$y = -0.048x^2 + 3.0074x + 4.213$		
9	SHS-M + VIR	Hf	Hf	0.97 / 0.25	$y = 4.87 \ln(x) + 3.78$		
10		Nb, Hf	Nb	2.01 / 1.00	$y = 8.89\ln(x) + 9.24$		
			Hf	3.47 / 0.90			
		Mo, Nb, Hf	Mo	4.06 / 2.00	$y = 8.27 \ln(x) + 11.11$		
11			Nb	1.96 / 1.00			
			Hf	3.39 / 0.90			
12	EC   IIID	Hf	Hf	0.96 / 0.22	$y = 5.33\ln(x) + 4.75$		
13	ES + HIP	Mo, Nb, Hf	Mo	7.93 / 4.00	$y = -0.2621x^2 + 16.896x + 29.971$		
			Nb	1.92 / 1.00			
			Hf	3.32 / 0.90			
		Mo, Nb, Hf	Mo	11.64 / 6.00			
14			Nb	1.88 / 1.00	$y = -0.6548x^2 + 44.62x + 17.681$		
			Hf	3.25 / 0.90			
15	HIP + HT	EP741NP			$y = -2.7111x^2 + 92.107x - 30.405$ $y = 29.95x + 234.17$		
16	nir + n i	AZhK			$y = 8.2829x^2 - 12.77x + 13.403$ $y = 34.27x + 31.89$		

microscope (SEM) S-3400N (Hitachi, Japan) with an energy dispersive spectrometer NORAN System 7 *X*-ray Microanalysis System (ThermoScientific, USA), and also on a transmission electron microscope (HRTEM) JEM-2100 (Jeol, Japan) using a Gatan 650 Single Tilt Rotation Analytical Specimen Holder (Gatan, Inc., USA). Samples (lamellae) were produced from pre-prepared foils using the focused ion beam (FIB) method on a Quanta 200 3D FIB instrument (FEI Company, USA).

HRTEM foils were obtained by ion etching on the PIPS II System instrument (Gatan Inc., USA).

### Results and discussion

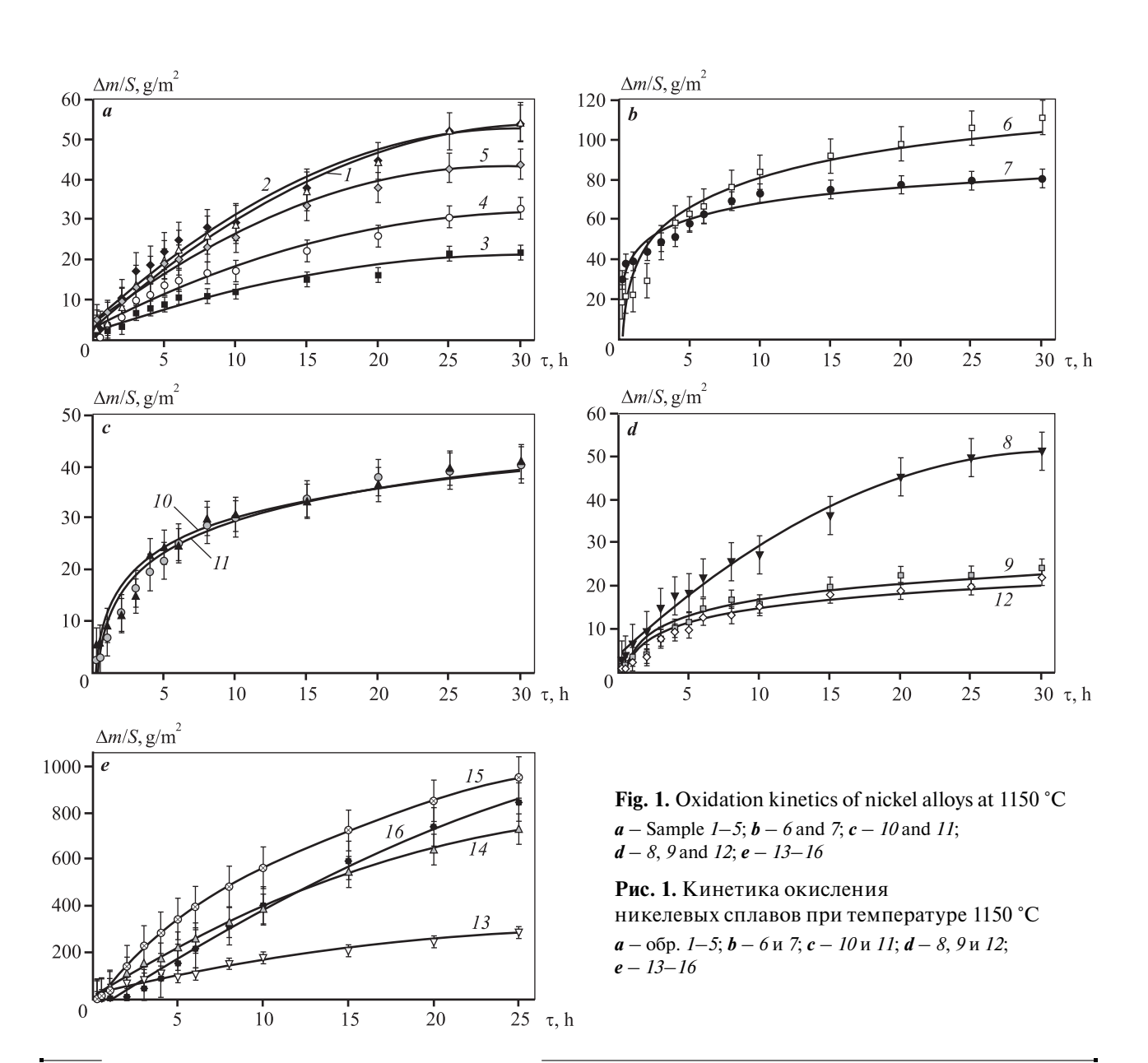
Analysis of kinetic curves and the composition of oxidation products described the influence of alloying additives on the solubility of oxygen, the course of polymorphic transformations and the formation of volatile suboxides. In contrast to simple metals, the interfaces of oxidized multicomponent intermetallic alloys are more complex. This is due to different chemical affinity to oxygen of alloying elements, the formation of multiple oxide phases and solid solutions, as well as different mobility of atoms in the oxide phase and the alloy.

Figure 1 shows the oxidation curves of the samples studied, and the above table provides their corresponding equations of approximation. The character of the curves corresponds to the parabolic law of oxidation for samples 1-5, 8, 13-14; to the logarithmic law for samples 6, 7, 9-12; and to the mixed law for samples 15, 16. In the latter case, at the initial stage (3-4 h) a parabol-

ic dependence was observed, and after violation of the sample integrity (Figure 2) the oxidation nature obeys a linear law and is controlled by the rate of the chemical reaction.

For samples 1-5, 8, 13 and 14, the highest oxidation rate is observed during the first 7-10 h. After the formation of a protective oxide layer, its values decrease and approach zero. Thus, the controlling oxidation process in this case is diffusion in a solid phase.

The oxidation process of samples 6 and 7 differs substantially from the others and is characterized by the action of additional factors associated presumably with the destruction of the external oxide layer due to



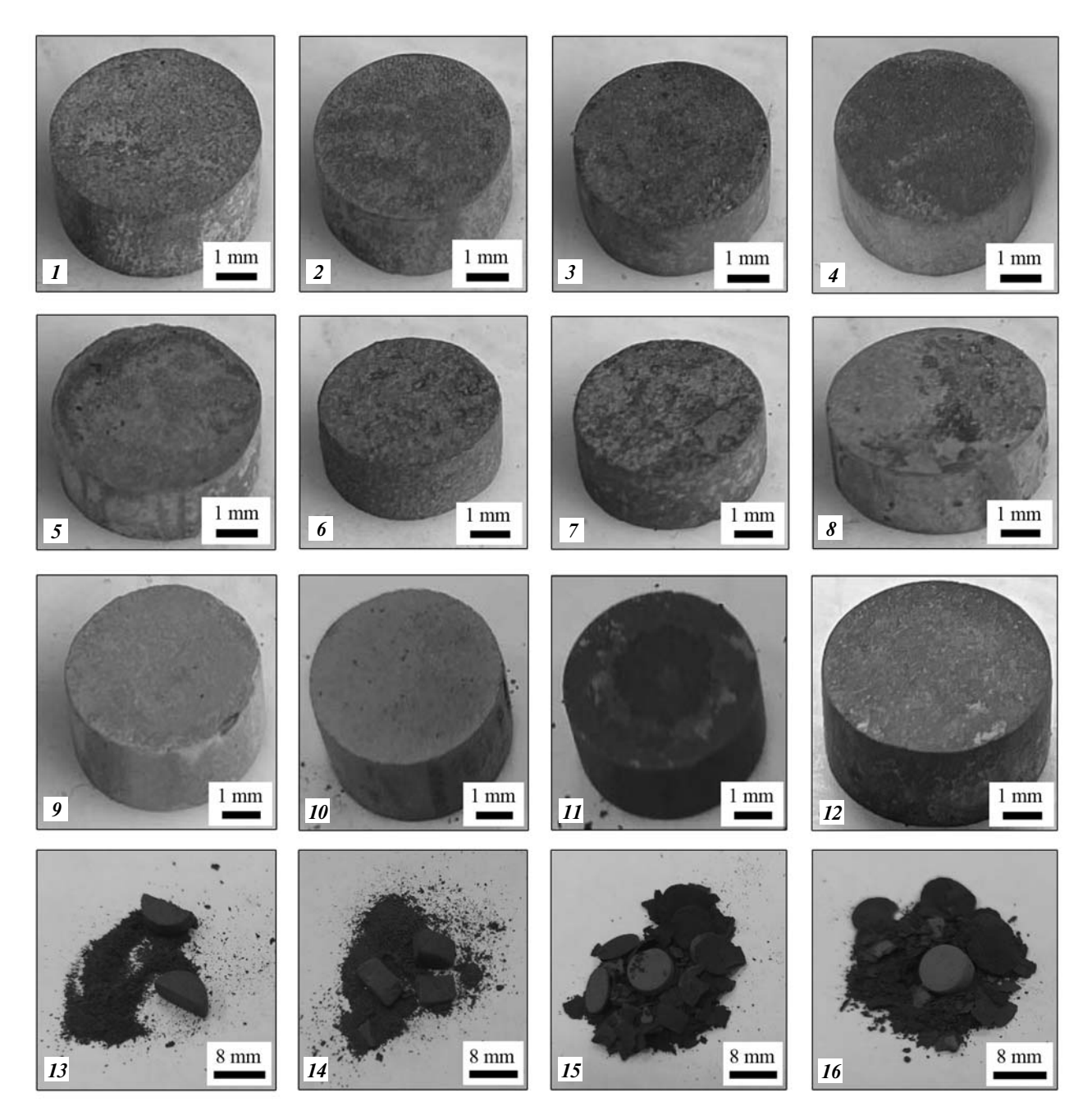


Fig. 2. Appearance of  $\beta$  alloys, EP741NP, AZhK samples after heat resistance tests at t = 1150 °C for 30 hours

**Рис. 2.** Внешний вид образцов из  $\beta$ -сплавов, ЭП741НП, АЖК после испытаний на жаростойкость при t = 1150 °C в течение 30 ч

internal stresses. This is confirmed by the change in their color and a friable surface, as seen in Figure 2. The oxidation kinetics of samples 9-12 depends on the content of molybdenum, niobium, hafnium and the size of the  $\beta$ -phase grains. The HfO<sub>2</sub> particles located at grain interfaces block the surface diffusion of aluminum and oxygen.

On the surface of oxidized samples, a layer with a certain relief and shade (see Figure 2) is visible. Visual analysis of samples 1-12 shows the absence of physical destruction. Samples 13 and 14 fractured in full due to the release of volatile molybdenum suboxides. At a lower content of Mo in the alloy (sample 11) the samples did not fracture.

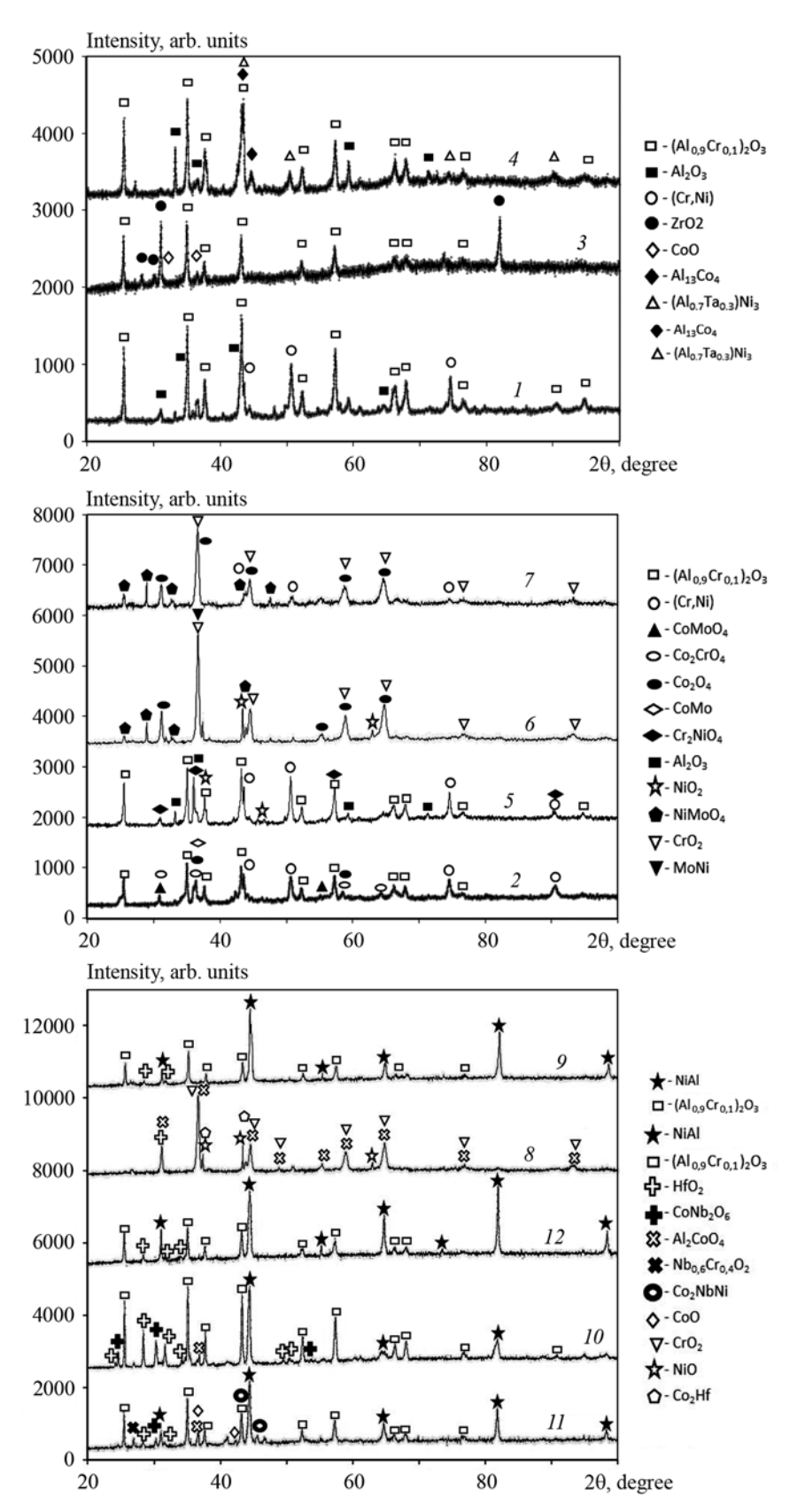


Fig. 3. XRD spectra of the oxidized surface of samples

Рис. 3. Дифракционные спектры окисленной поверхности образцов

Samples 15 and 16 from alloys EP741NP and AZhK also fractured completely. As a result of diffusion there is a high concentration of excess vacancies under the oxide layer. When critical thickness is reached, there is gradual cracking of the film with transformation into a loose oxide. The operating temperatures of parts made of these alloys are limited to the interval of 750—800 °C [28], which is noticeably lower than the test temperature

of 1150 °C. However, our work was aimed at a comparative analysis of the oxidation kinetics of a group of alloys under the same conditions.

The diffraction spectra of the surface of  $\beta$ -alloys, oxidized at t = 1150 °C for 30 h, are shown in Figure 3. The main peaks correspond to the nickel monoaluminide (NiAl) phase as the alloying additives pass into a solid solution. The main oxidation prod-

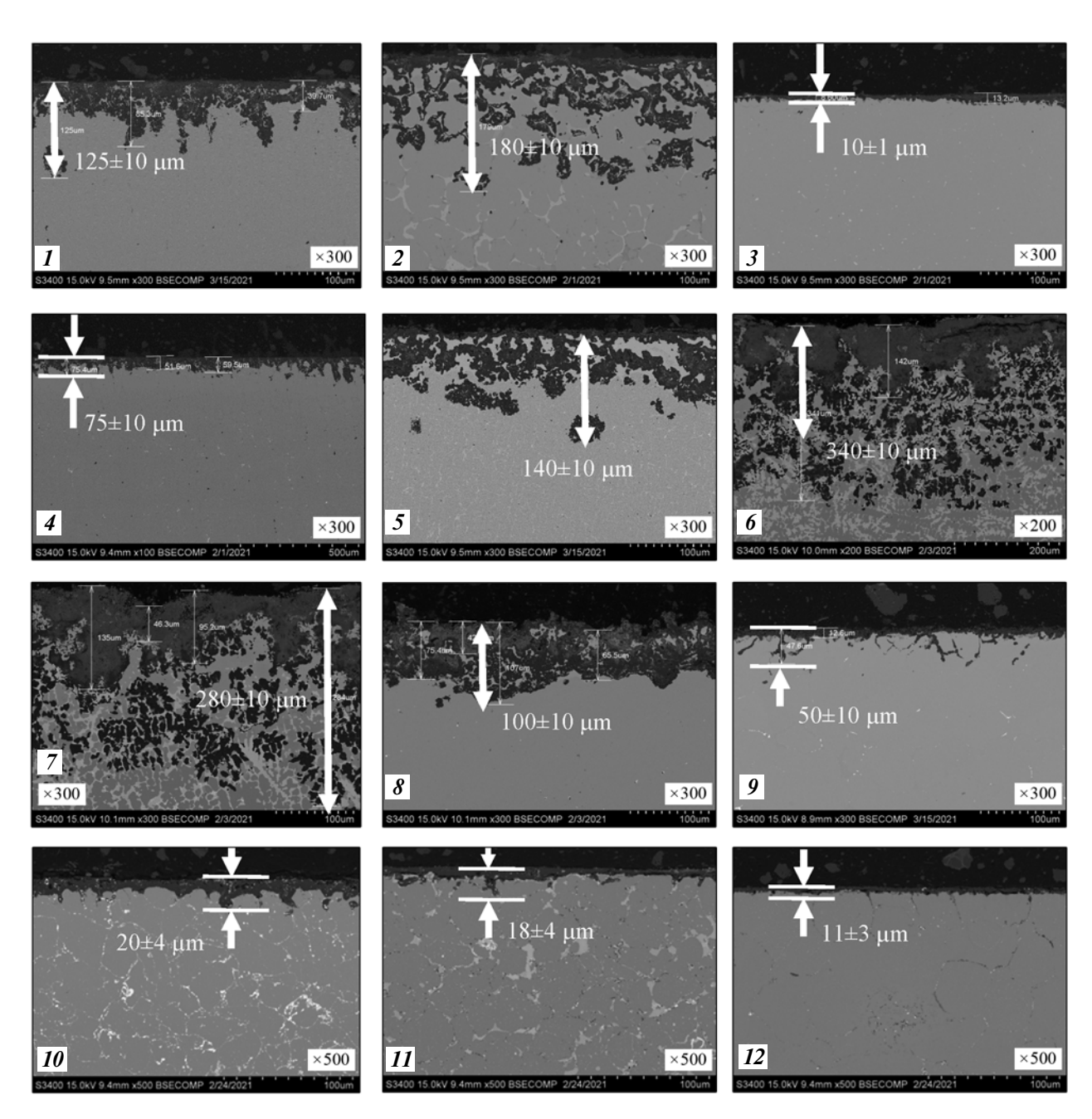


Fig. 4. Microstructures of alloys indicating the oxidized layer thickness

Рис. 4. Микроструктуры сплавов с указанием толщины окисленного слоя

uct is  $\gamma$ -Al<sub>2</sub>O<sub>3</sub>, and some accompanying oxides are present.

Figure 4 shows the microstructures of oxidized and transition layers of the study samples with the indication of typical thicknesses. A feature of the alloys under study with different alloying systems is the formation of a continuous, tightly adhering oxide film at the initial oxidation stage. This inhibits the diffusion penetration of oxygen and nitrogen to the metal. The analysis of the MeO—Me transition layer indicates

diffusion of oxygen and nitrogen. The data presented in Figure 4 shows the influence of alloying elements, the molybdenum (2.5—15.0 at.%) and hafnium content (0.25—0.9 at.%), as well as the alloy production method (SHS-M, VIR, ES, HIP) on the oxidation depth and thickness of the transition Me—MeO layer. A more detailed analysis for each composition is presented in Figures 5—17.

Sample *1* has a considerably lower (in comparison with calculation) content of lanthanum. This is due to

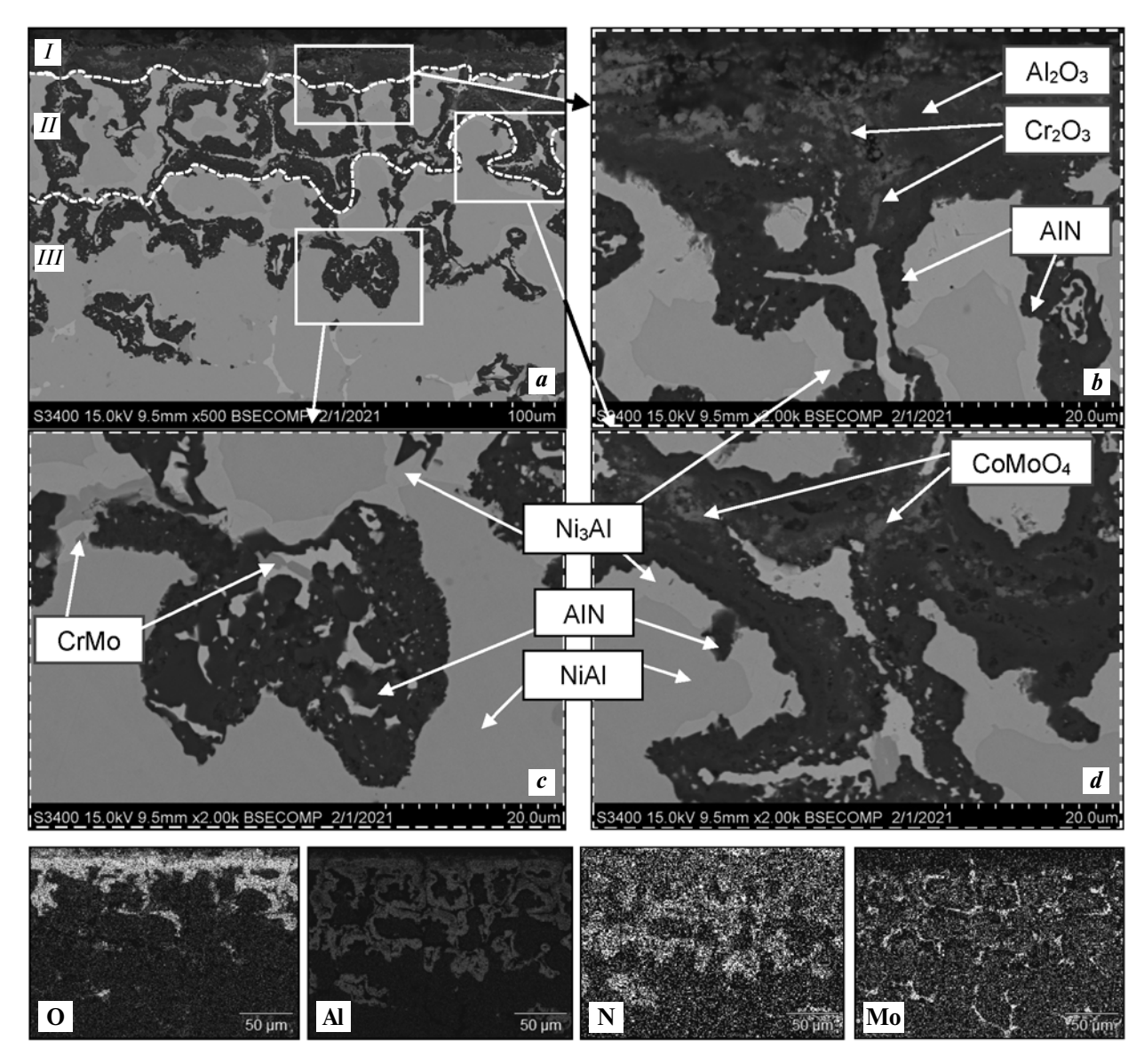


Fig. 5. Microstructure (a), marked analysis areas (b-d) and map of oxidized layer element distribution in Sample 2 (see table)

**Рис. 5.** Микроструктура (a), выделенные области анализа (b-d) и карта распределения элементов окисленного слоя в обр. 2 (см. таблицу)

its high affinity to oxygen, participation in the reduction metallothermic reaction during synthesis and partial transition into a slag phase [26]. Therefore, the alloy with low lanthanum content was excluded from further studies.

Figure 5 shows microstructures of the oxidized layer of sample 2 with molybdenum. Diffusion of oxygen and nitrogen occurs predominantly at grain interfaces and intergranular interlayers of phases containing Cr—Mo. At the NiAl—MeO interfaces, the Ni<sub>3</sub>Al phase can be

observed as a result of Al<sub>2</sub>O<sub>3</sub> formation and aluminum depletion of the NiAl phase.

Analysis of samples after 30 h of testing shows the Me—MeO transitional layer. At the initial stage there is reactive diffusion of oxygen along the grain interfaces of the  $\beta$ -phase solid solution with the formation of a solid Al<sub>2</sub>O<sub>3</sub> and Cr<sub>2</sub>O film. At the same time, nitrogen also diffuses deep into the sample, reacting with aluminum to form AlN, and depleting NiAl to Ni<sub>3</sub>Al (light gray areas). In the molybdenum-doped alloy, maximum thick-

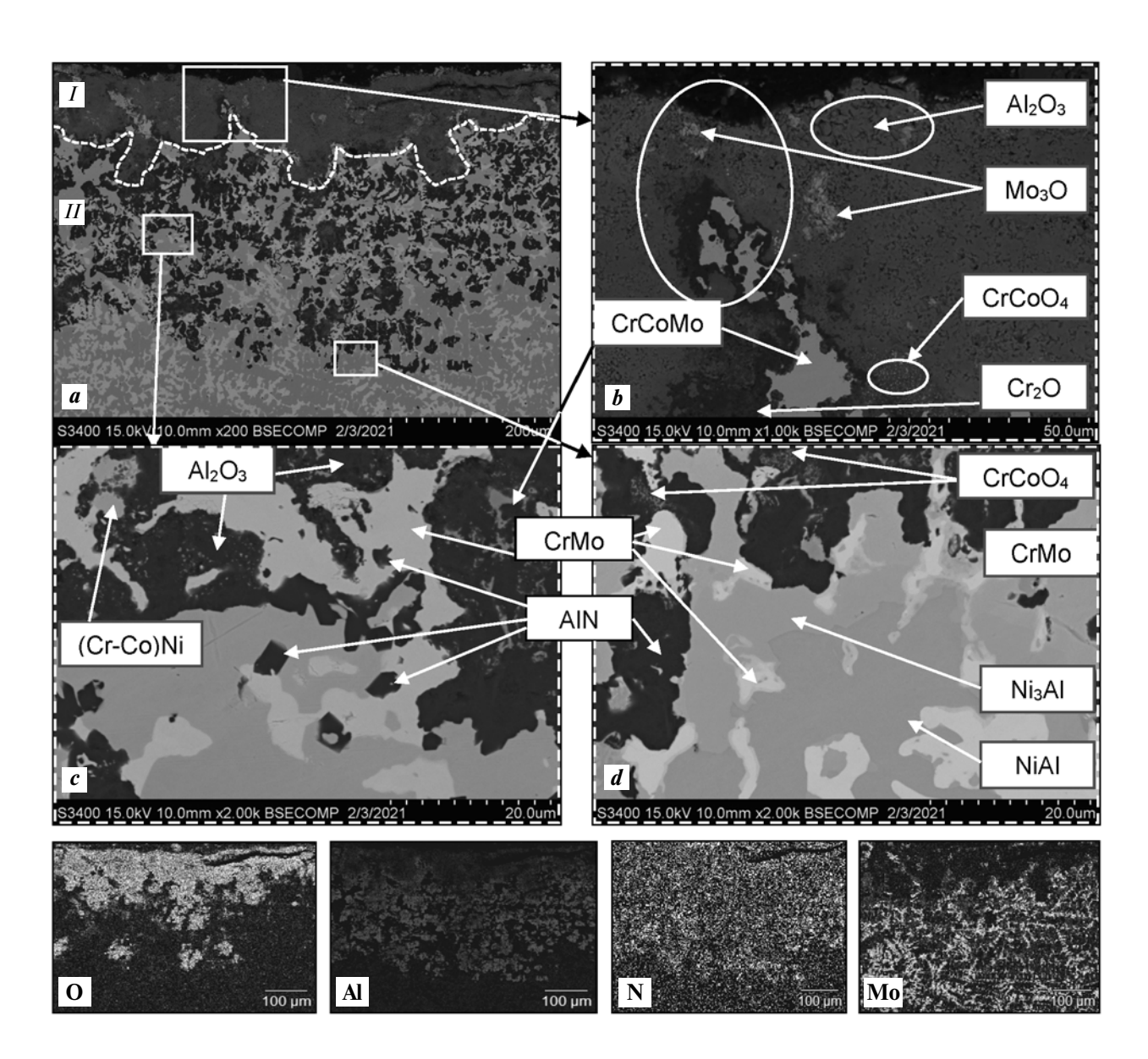


**Fig. 6.** Microstructure (a), marked analysis areas (b-d) and map of oxidized layer element distribution in Sample b **Puc. 6.** Микроструктура (a), выделенные области анализа (b-d) и карта распределения элементов окисленного слоя в обр. b

ness of the transition layer can be observed (see Figure 4). Molybdenum in oxidation forms oxides  $MoO_3$ ,  $Mo_3O_4$  and  $CoMoO_4$ , which sublimate and lead to periodic destruction of the integrity of the protective layer. This then contributes to the diffusion of new portions of active nitrogen and oxygen ions.

Thus, this cyclic mechanism is used to move the oxidation front deep into the sample, as confirmed by the studies of sample 6 with an increased content of molybdenum, the results of which are shown in Figures 4 and 6.

A characteristic difference of sample 6 is penetration of oxygen and nitrogen to the depth of up to  $340\pm10~\mu m$  (see Figure 4). In Figure 6, we can identify the appearance of more areas of oxide and nitride components. In addition, the burning out of molybdenum in the form of suboxides affects the thickness of the surface oxide layer:  $20\pm5~\mu m$  for sample 2; and  $130\pm5~\mu m$  for sample 6. A distinctive feature of the oxidation kinetics of the latter is the more intense inhibition of the film growth over time according to the logarithmic law. Oxidation

starts at a high rate, but its value quickly decreases and is further controlled by the process of electron transfer through the oxide film.

Figure 7 shows the characteristic microstructures of the MeO—Me transition layer in sample 4 with tantalum. The analysis of the kinetic curves of high-temperature oxidation revealed that the modification with tantalum makes a positive result, slowing down the oxidation rate (see Figure 1, a).

Distribution of oxygen and nitrogen in the oxidized layer can be conventionally divided into three sublayers: I — solid oxide film of  $Al_2O_3$  with  $Ta_2O_5$ ,  $Cr_2O_3$  inclusions and a small amount of AlN; II — oxides with predominantly AlN content; III — metallic layer with nitride inclusions and without oxides.

Tantalum located in the intergranular space is oxidized to  $Ta_2O_5$ . Compared to the Mo-containing system, the  $\beta$ -phase depletion to  $Ni_3Al$  does not occur. A detailed study of the structure of the Ta-containing alloy [26] established the concentration shift of chromium dissolved in the  $\beta$ -phase solid solution to the grain

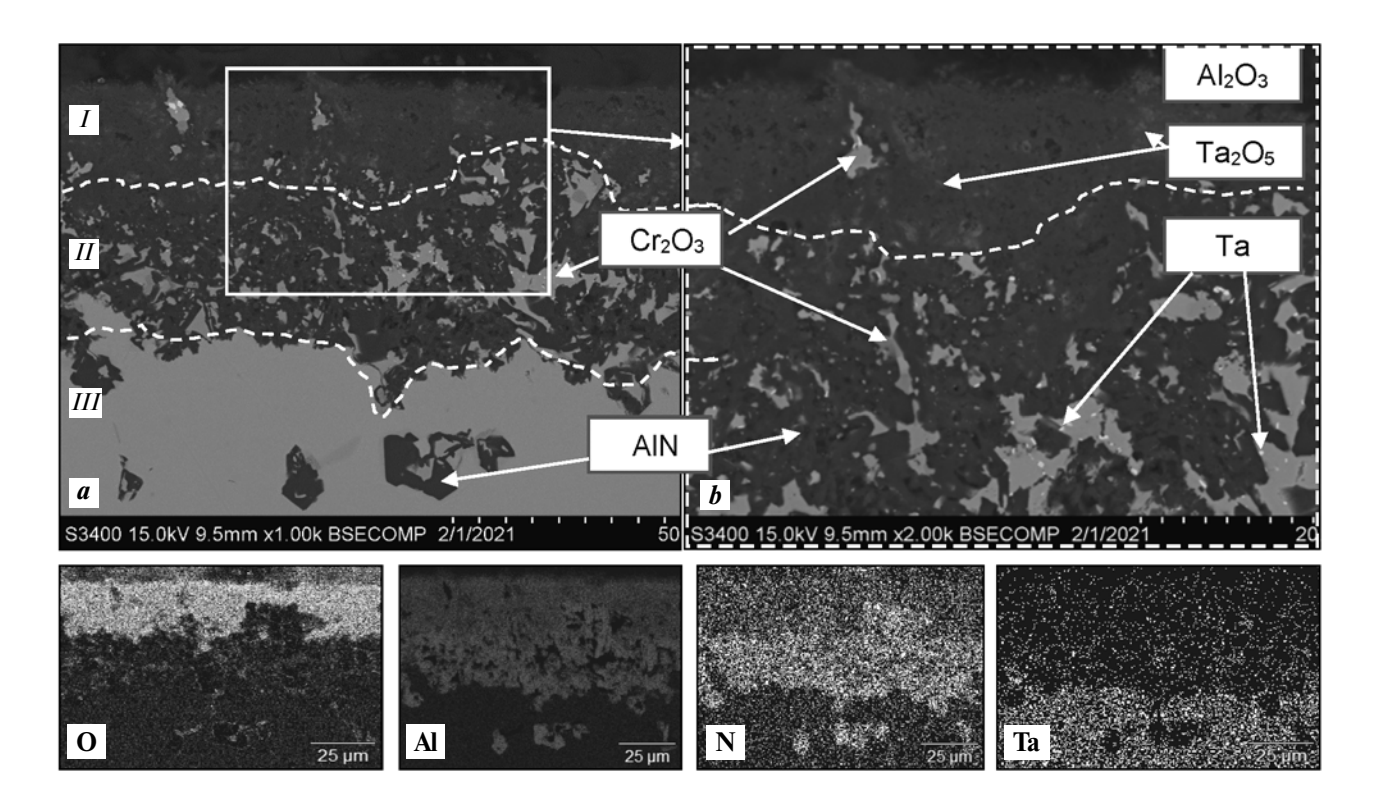


**Fig. 7.** Microstructure (*a*), marked analysis area (*b*) and map of oxidized layer element distribution in Sample *4* **Puc. 7.** Микроструктура (*a*), выделенная область анализа (*b*) и карта распределения элементов окисленного слоя в обр. *4* 

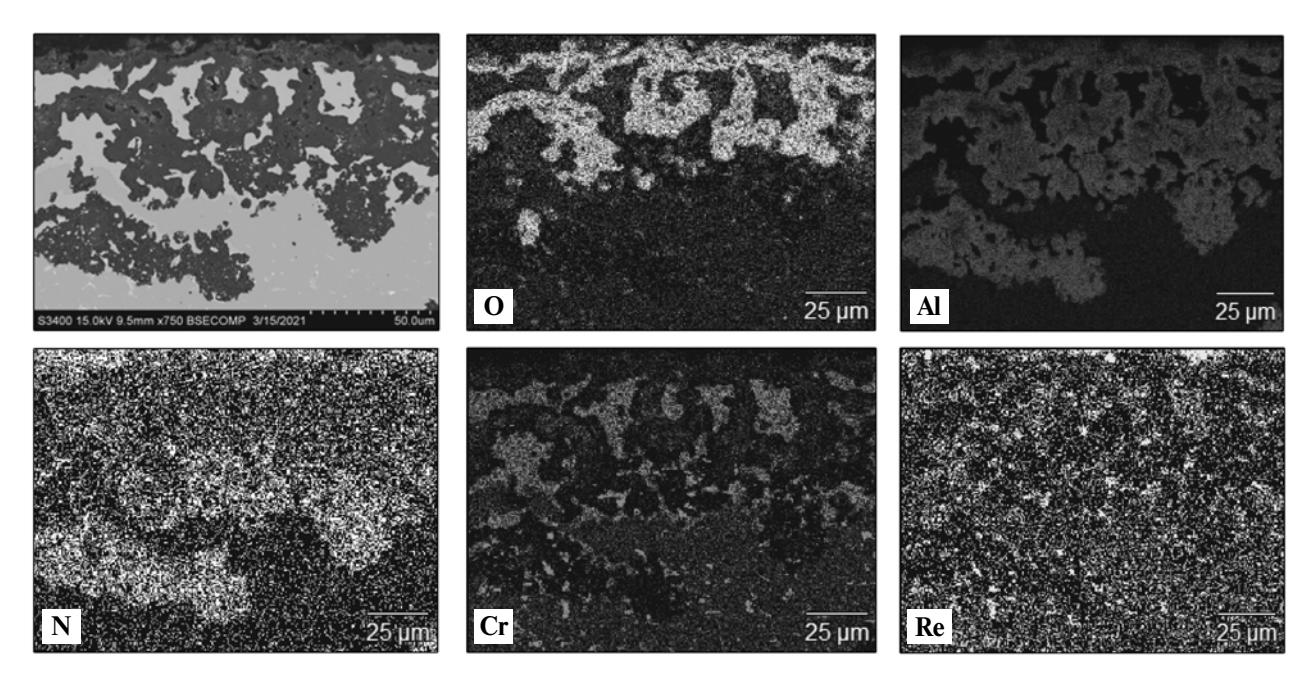


Fig. 8. Microstructure and map of oxidized layer element distribution in Sample 5

Рис. 8. Микроструктура и карта распределения элементов окисленного слоя в обр. 5

interfaces. Thus, in the first place, chromium interacts with oxygen to form a volatile oxide. It is due to these two distinctive features that the oxidation rate is reduced.

In the comparative analysis of sample 3 with the basic composition, a slight slowdown of oxidation processes can be observed (see Figure 1, a, d). The reason for the decrease in the oxidation rate can be traced from microstructures and the elements distribution map of the MeO—Me transition layer presented in Figure 7. As shown above, in the parabolic dependence, diffusion along the interfacial boundaries is the controlling process.

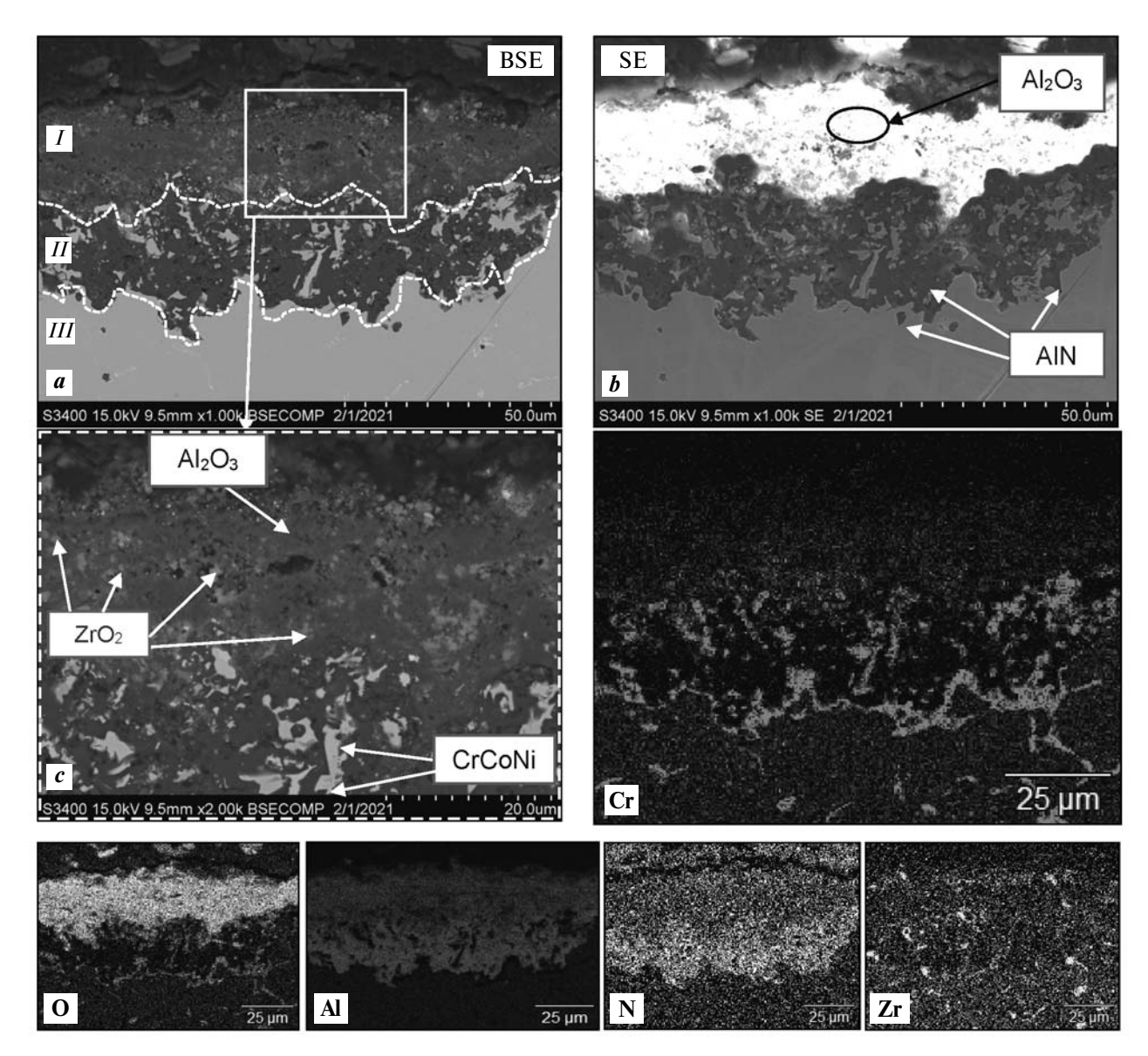
The total depth of the oxidized layer decreases as the size of the structural components decreases, the grain interfaces branch and the diffusion path increase. This is confirmed in the case of rhenium-modified alloy (see Figure 1, a). Figure 1, b shows the comparison of kinetic oxidation curves for samples b and b. This also confirms a decrease in the dynamics of oxidation processes with additional alloying with rhenium. The oxidation of alloys with rhenium does not form a dense layer of b0 on the surface, which has a negative effect on the heat resistance. The main recommendation in this case is to use combined alloying, in order to introduce, along with rhenium, an element that inhibits oxidation processes, such as zirconium.

Figure 9 shows microstructures of the oxidized layer

of sample 3 with zirconium. This alloying system showed the best result in a series of experiments (see Figure 1, a). The SEM images of the cross section of oxidized sample 3 are shown in Figures 9 and 10. The thickness of the oxidized layer was  $10\pm 5~\mu m$ , which is an order of magnitude smaller than in the other samples. In Figure 9, we can identify the  $Al_2O_3$  layer with inclusions of chromium-cobalt oxide phases characteristic of all samples. The white light dots distributed throughout the oxidized layer correspond to the  $ZrO_2$  phase. Nanosized  $ZrO_2$  formations are present in the main  $Al_2O_3$ -based layer (see Figures 9, c and 10).

Analysis of Figure 10 shows that under the  $Al_2O_3 + ZrO_2$  layer there is a thin continuous film of  $Cr_2O_3$ , which is typical for this alloying system. The upper oxide layer of  $Al_2O_3 + ZrO_2$  presumably inhibits the external diffusion of oxygen and nitrogen, and also blocks the sublimation of volatile chromium oxide  $Cr_2O_3$ . Thus, it gradually forms a dense layer across the Me—MeO transition surface, forming a second continuous barrier oxide layer.

The oxide layer of sample 3 with zirconium after heat-resistance tests was chosen for the analysis by HRTEM and electron beam diffraction on a JEM-2100 microscope (Jeol, Japan). Figure 11 shows an image of the alloy structure and the oxide layer formed, as well



**Fig. 9.** Microstructure (a), marked analysis areas (b, c) and map of oxidized layer element distribution in Sample  $\beta$  **Puc. 9.** Микроструктура (a), выделенные области анализа (b, c) и карта распределения элементов окисленного слоя в обр.  $\beta$ 

as a map of distribution of the main elements therein. Between the NiAl matrix layer and the outer oxide layer there is a layer of the Ni<sub>3</sub>Al phase with evenly distributed inclusions of Co, Cr, and  $Cr_2O_3$ . The upper oxide layer consists of  $Al_2O_3$  with inclusions of  $ZrO_2$  (dark gray areas), confirming the results of the EDX analysis (Figure 12, spectra 1, 3, 4). Based on the quantitative ratio of the main components in spectral region 2 (Figure 12), the phase was investigated by HR TEM and electron beam diffraction, thus establishing the phase of complex oxide  $Zr_5Al_3O_{0.5}$  (Figure 13).

The  $Zr_5Al_3O_{0.5}$  phase has a hexagonal crystal lattice (space group  $P6_3mc$ ). The lattice periods of the  $Zr_5Al_3O_{0.5}$  phase, calculated on the basis of the electron diffraction pattern, with regard to the Miller indices are: a = 14.153 Å, c = 5.671 Å.

Thus, high-temperature oxidation produces a complex oxide in the form of nano-sized crystallites  $Zr_5Al_3O_{0,5}$  impregnated into the  $Al_2O_3$  layer. This combination reduces the catalytic activity and positively affects the oxidation resistance of the alloy at t = 1150 °C.

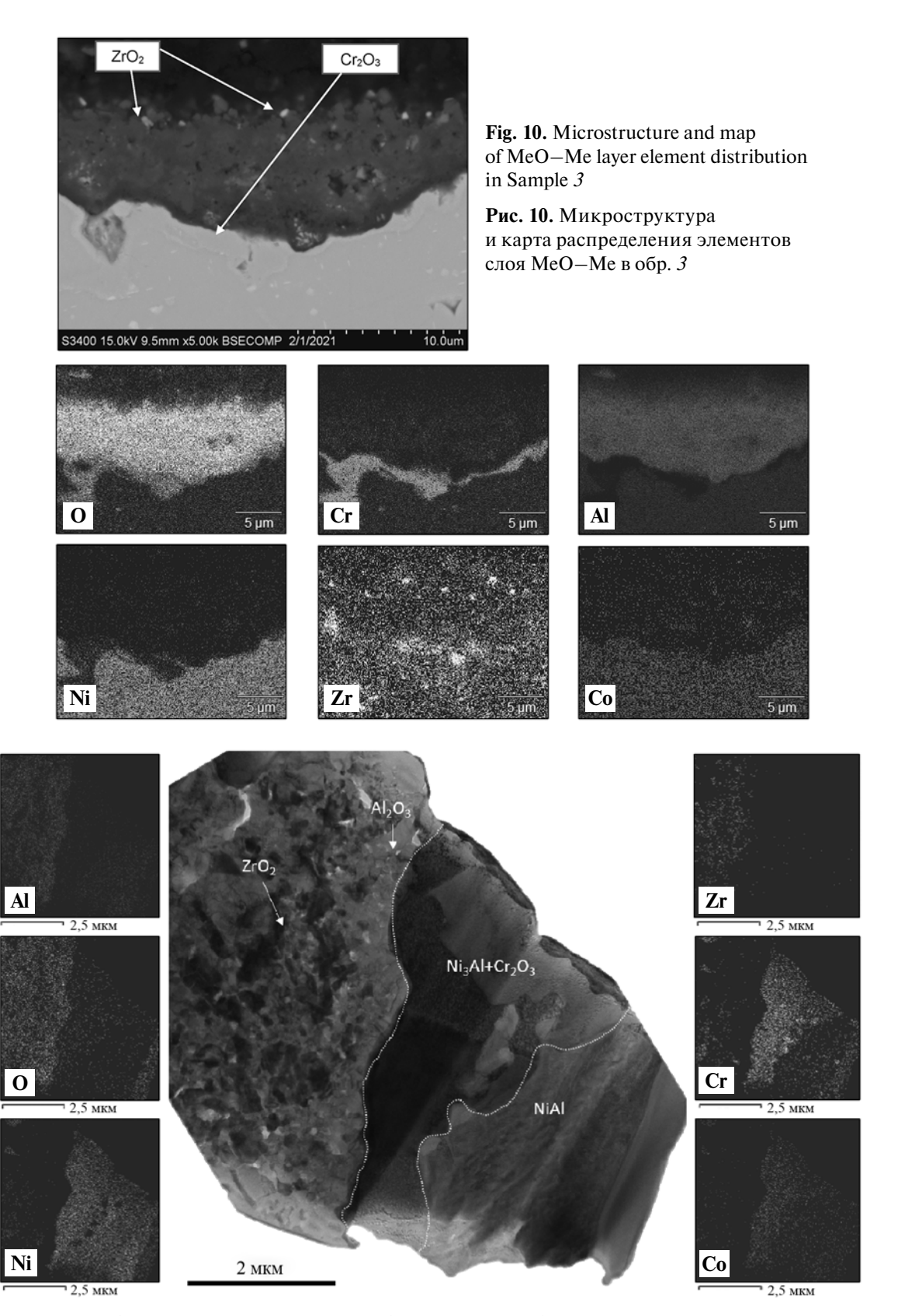
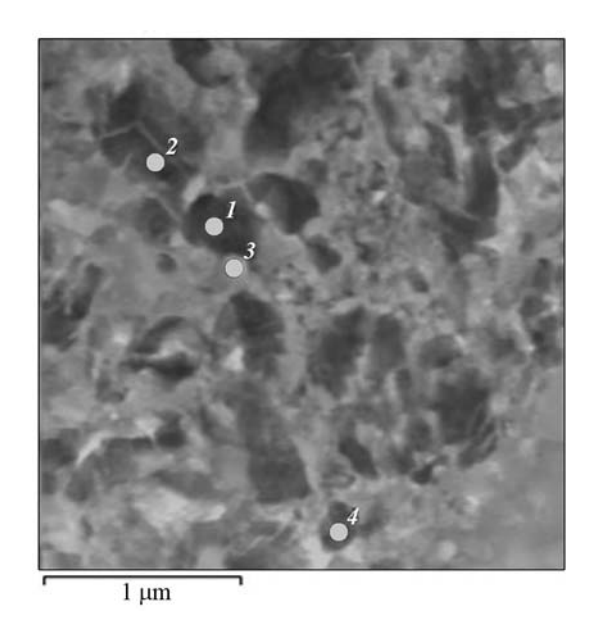


**Fig. 11.** TEM image of Sample 3 structure, oxide layer formed and map of main element distribution **Puc. 11.** ПЭМ-изображение структуры обр. 3 и образовавшегося оксидного слоя, а также карта распределения основных элементов



Spectrum	О	Al	Cr	Co	Ni	Zr
1	54.65	3.93	_	-	-	41.42
2	45.28	23.69	_	_	_	31.04
3	56.35	37.55	3.91	0.46	0.78	0.95
4	58.27	3.22	_	_	_	38.51

**Fig. 12.** Chemical composition (at.%) of boundary oxide layer regions

**Рис. 12.** Химический состав (ат.%) областей пограничного оксидного слоя

Comparative analysis of oxidation curves (see Figure 1, d), as well as the composition and microstructure of oxidized samples (Figures 14, 15) from the basic  $\beta$ -alloy, obtained by different process flowcharts: SHS-M [18] (Figure 8), SHS-M + VIR [18, 19] (Figure 9), ES with subsequent spheroidization of the powder and HIP [20] (sample 12), showed that the technology used has an effect on their heat resistance. Figure 1, d shows the difference in the oxidation kinetics of sample  $\delta$  (SHS-M) from samples  $\theta$  and  $\delta$  subjected to additional after-treatment.

Analysis of the microstructure (see Figures 4, 14) of the transition layer of samples  $\delta$  (SHS-M) and  $\delta$  (SHS-M + VIR) demonstrates a 2-fold difference in the thickness of the oxide and transition layers:  $100\pm10$  and  $50\pm10$  µm, respectively. In sample  $\delta$  (SHS-M + VIR), the AlN phase is not formed in the MeO—Me transition layer, indicating that the metal is refined during VIR [19]. The impurity nitrogen content in samples  $\delta$  and  $\delta$  is [N] = 0.0044 and 0.00083 wt.%, respectively. Its reduction leads to a different oxidation mechanism similar to that of sample  $\delta$ . Here a dense protective  $\delta$  crack sublayer is formed under a loose  $\delta$  and  $\delta$  layer. In this oxidation mechanism, diffusion occurs only at phase interfaces and penetrates deep into the sample in the form of weedges» (see Figure 14,  $\delta$ ).

The VIR process is a useful way of refining alloys from detrimental impurities. However, it also has some

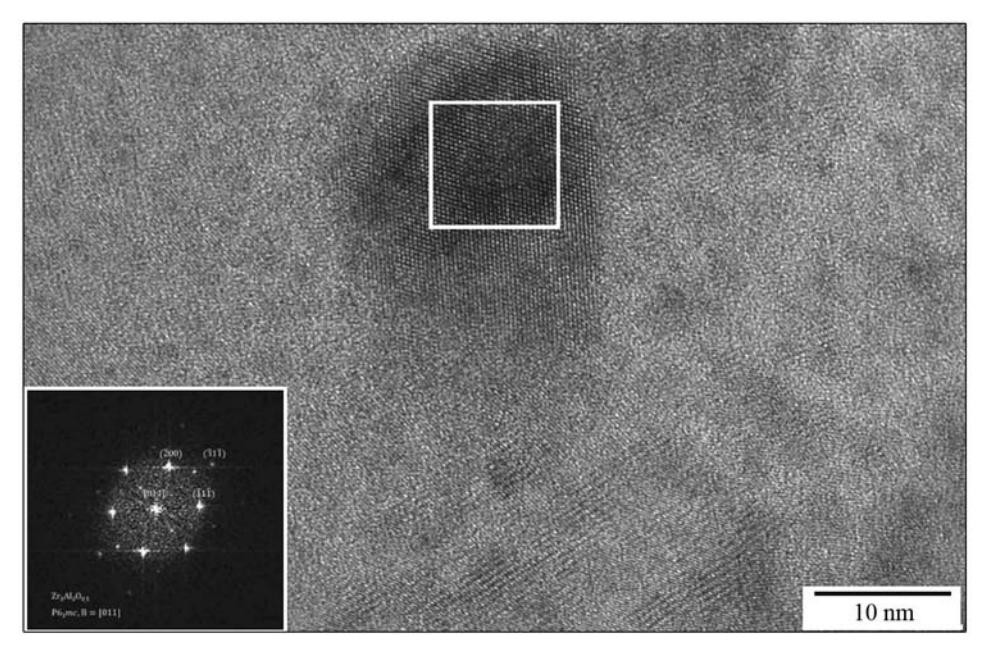


**Fig. 13.** TEM image of the  $Zr_5Al_3O_{0.5}$  phase with an electron diffraction pattern along the zone [011] axis **Puc. 13.** ПЭМ-изображение фазы  $Zr_5Al_3O_{0.5}$  с электронограммой вдоль оси зоны [011]

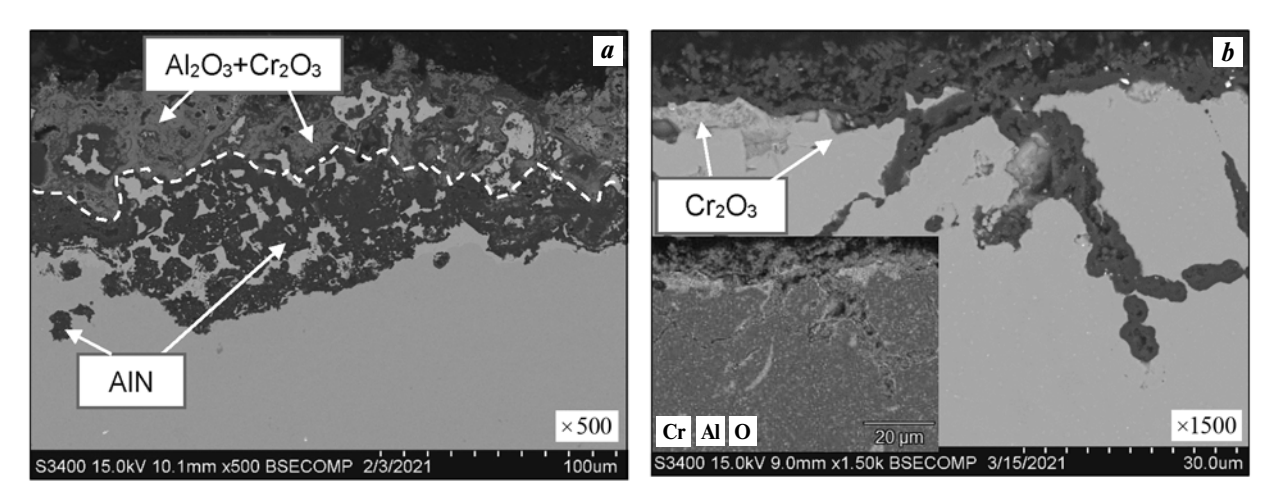


Fig. 14. Microstructure of the oxidized layer of Sample  $\delta$  (SHS-M) (a) and Sample  $\theta$  (SHS-M + VIR) (b)

**Рис. 14.** Микроструктура окисленного слоя образцов  $\delta$  (CBC-M) (*a*) и  $\theta$  (CBC-M + ВИП) (*б*)

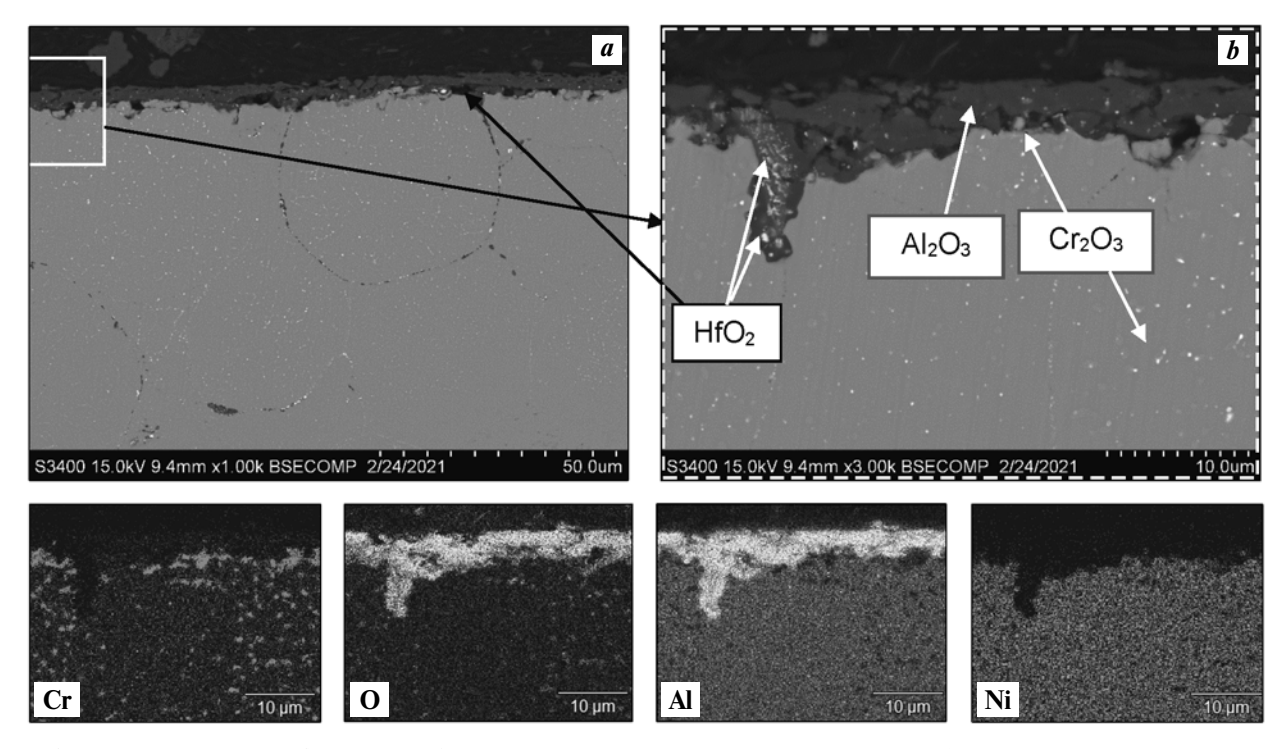


Fig. 15. Microstructure  $(a, \delta)$  and map of oxidized layer element distribution in Sample 12 (ES + HIP)

**Рис. 15.** Микроструктура (a,  $\delta$ ) и карта распределения элементов в окисленном слое обр. 12 (ЭС + ГИП)

drawbacks described in [18—20]. A more efficient and less energy-consuming method for refining cast SHS alloys is vacuum annealing at t = 0.7tm, which removes up to 70 % of impurity nitrogen and hydrogen. The reduction of residual oxygen content is possible only during full metallurgical processing (VIR). Sample 12 (ES + HIP) has similar kinetics to sample 9 (see Figure 1, d), while the mechanisms of counteracting the

diffusive penetration of oxygen and nitrogen are different.

The impurity oxygen content in these systems is  $[O] \le 0.12$  wt.%. [20]. The oxidation process in the alloy begins at the interfaces of the consolidated powders. The element distribution map demonstrates the distribution areas of  $Al_2O_3$  and  $Cr_2O_3$  oxides, contributing to the destruction of samples, along with

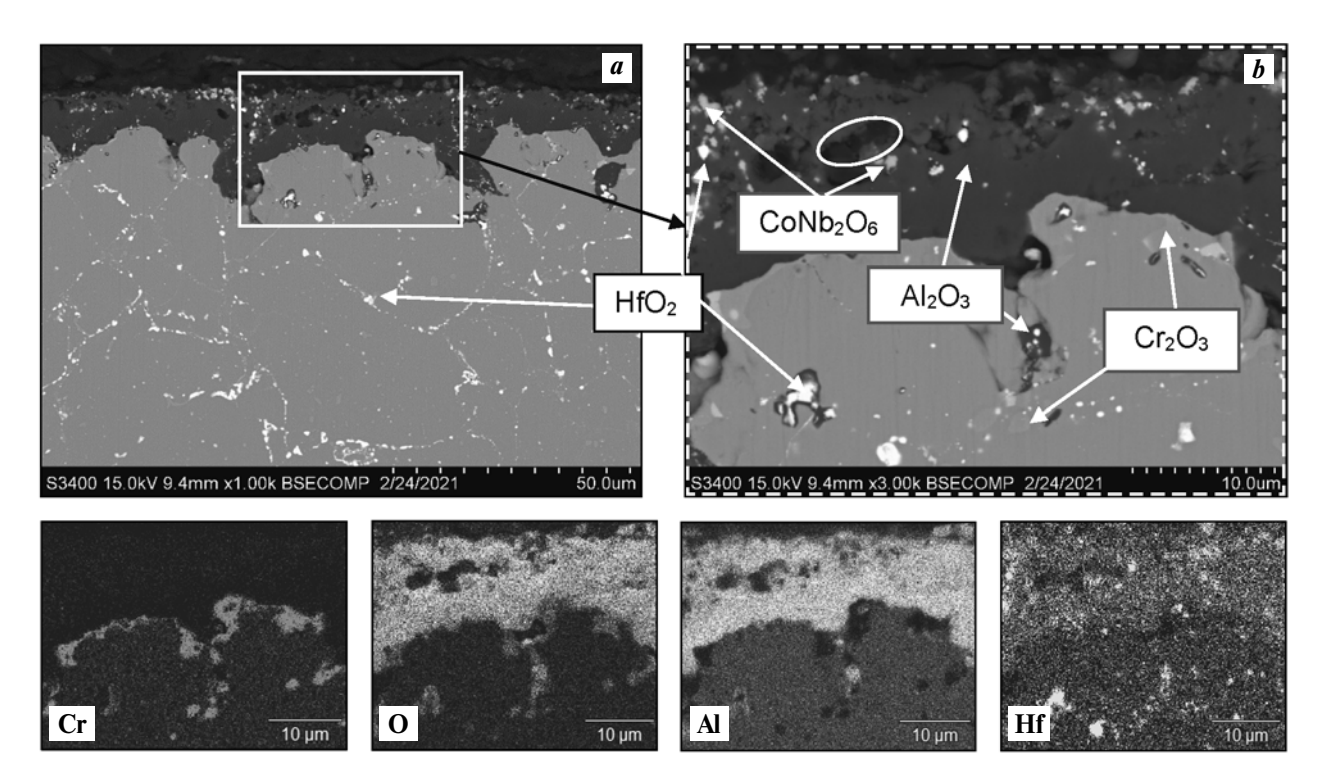
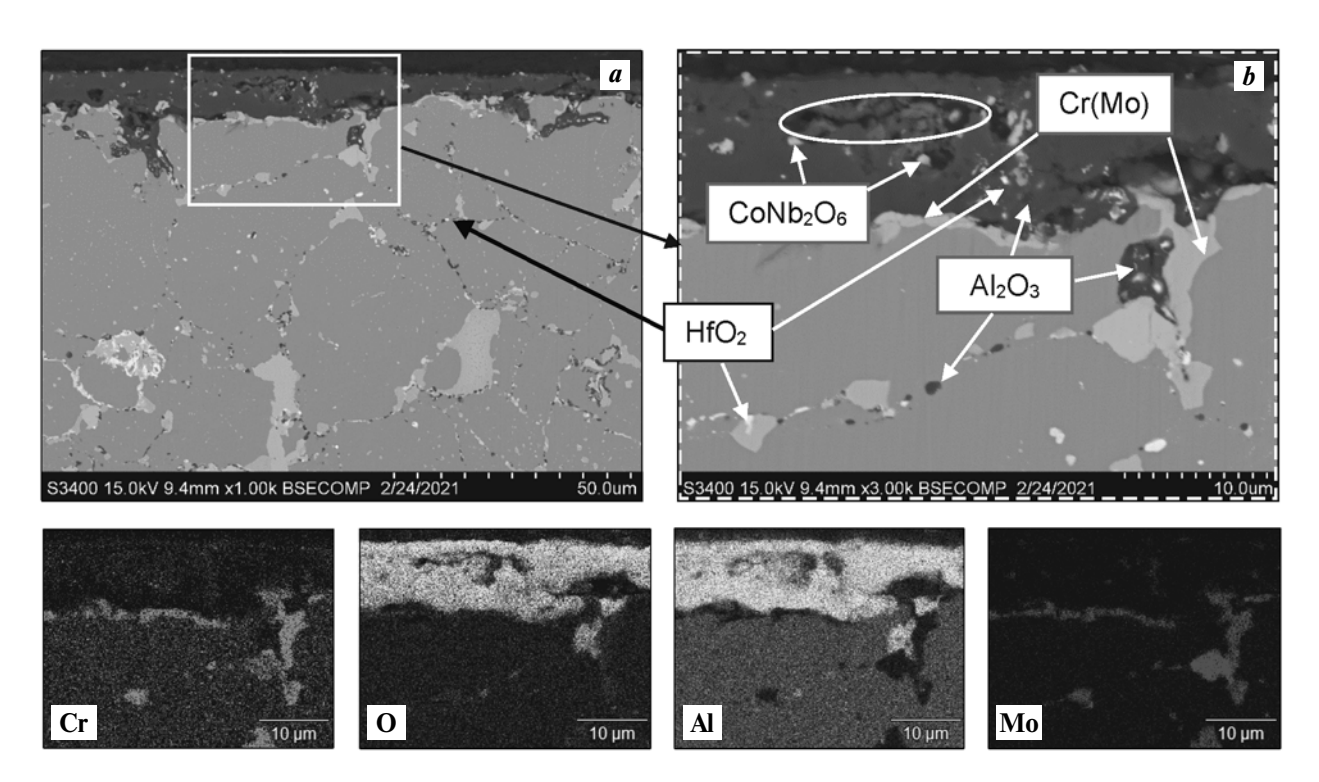


Fig. 16. Microstructure  $(a, \delta)$  and map of oxidized layer element distribution in Sample 10 (ES)

**Рис. 16.** Микроструктура (a,  $\delta$ ) и карта распределения элементов окисленного слоя в обр. 10 (ЭС)



**Fig. 17.** Microstructure  $(a, \delta)$  and map of oxidized layer element distribution in Sample 11 (ES)

**Рис. 17.** Микроструктура (a,  $\delta$ ) и карта распределения элементов окисленного слоя в обр. 11 (ЭС)

the action of volatile molybdenum oxides (samples 13 and 14).

The mechanisms of protection against external diffusion of oxygen and nitrogen in sample 12 (ES + HIP) and 9 (SHS + VIR) are similar and depend on the formation of a thin protective film of  $\rm Cr_2O_3$ . When the nitrogen content in the sample is less than 0.0017 wt.%, the AlN phase is not formed during oxidation [25]. In finegrained samples (ES + HIP) [25], the limiting factor for oxygen penetration deep into the sample is a branched system of grain interfaces.

Figures 16 and 17 show the microstructures of the oxidized layer of samples 10 and 11 obtained by the ES method [27]. Comparing the kinetic functions of their oxidation to the SHS-M samples, similar patterns can be noted. However, analysis of the microstructures showed that their oxidation mechanisms are somewhat different. The primary layer consists of Al<sub>2</sub>O<sub>3</sub> with inclusions of HfO<sub>2</sub>, CoNb<sub>2</sub>O<sub>6</sub>, but in the oxide layer the pores noted in Figures 16 and 17 are formed by evaporation of volatile niobium and molybdenum suboxides. The latter destroy the primary Al<sub>2</sub>O<sub>3</sub> layer, leading to intense oxidation at the initial stage (see Figure 1, c). Larger niobium inclusions in the oxide layer of the alloy form the CoNb<sub>2</sub>O<sub>6</sub> phase. Hafnium oxide HfO2 is uniformly distributed as submicron and nanoscale inclusions along the grain interfaces, thereby suppressing oxygen diffusion inside nickel aluminide [29]. In sample 10, a thin protective layer of Cr<sub>2</sub>O<sub>3</sub> is observed under the Al<sub>2</sub>O<sub>3</sub> layer.

In alloy 11 the Cr(Mo) solid solution phase is also located at the grain interfaces along with  $HfO_2$  inclusions. The initial oxidation period is similar to that of sample 10. However, due to the molybdenum there is more active oxygen diffusion deep into the sample at the grain interfaces with the formation of  $Al_2O_3$  and volatile  $MoO_3$ , which are sublimated and do not impede further oxygen penetration.

### Conclusion

1. Kinetic curves were constructed and equations corresponding to them were established for approximation of the oxidation process at t = 1150 °C for 30 h of various heat resistant nickel alloys based on nickel monoaluminide obtained by centrifugal SHS metallurgy (SHS-M), vacuum induction remelting (VIR), elementary synthesis (ES) and hot isostatic pressing (HIP).

Depending on the alloy composition and the method of its production, the nature of the curves corresponds to parabolic, logarithmic or mixed oxidation laws.

In the case of alloys AZhK and EP741NP, at the initial stage (3—4 h) a parabolic dependence is observed, and after violation of the sample integrity the oxidation character obeys a linear law and is controlled by the rate of the chemical reaction.

**2.** Alloying interstitial elements contribute to the growth of oxidation resistance of  $\beta$ -alloys. This is due to the formation of additional phases. In the sample (SHS-M) alloyed with tantalum, the Ta<sub>2</sub>O<sub>5</sub> phase is formed in the intergranular space, which reduces the oxidation rate and depth.

A zirconium-doped sample (SHS-M) showed the best result: the degree of oxidation for 30 h was  $21 \text{ g/m}^2$ . The zirconium-containing top layer of  $Al_2O_3$  +  $Zr_5Al_3O_{0.5}$  blocks the external diffusion of oxygen and nitrogen, thereby increasing the heat resistance.

Hafnium alloying causes the formation of submicron and nanoscale inclusions of HfO<sub>2</sub> at the grain interfaces, suppressing the grain interface diffusion of oxygen, and a thin protective Cr<sub>2</sub>O<sub>3</sub> layer is formed under the Al<sub>2</sub>O<sub>3</sub> layer.

In alloys with molybdenum volatile oxides of  $MoO_3$ ,  $Mo_3O_4$ , and  $CoMoO_4$  are formed which destroy the integrity of the protective layer. As the concentration of molybdenum increases, the depth of oxygen and nitrogen penetration increases, too.

3. Comparative analysis of the kinetics and mechanism of oxidation of basic  $\beta$ -alloy samples with chromium, cobalt and hafnium additions showed a significant effect on the heat resistance of the method of obtaining samples. The oxidation mechanism also changes with the reduction of the percentage of impurity nitrogen and formation of the  $Cr_2O_3$  sublayer.

Acknowledgments: The research was funded by the Ministry of Science and Higher Education of the Russian Federation (Government Task Project No. 0718-2020-0034).

Работа выполнена при финансовой поддержке Министерства науки и высшего образования Российской Федерации (проект государственного задания № 0718-2020-0034).

### References

1. *Логунов А.В.* Жаропрочные никелевые сплавы для лопаток и дисков газовых турбин. М.: ИД «Газотурбиные технологии», 2017.

- Logunov A.V. Heat-resistant nickel alloys for blades and disks of gas turbines. Moscow: «Gazoturbinnye tekhnologii», 2017 (In Russ.).
- Hu L., Zhang G., Hu W., Gottstein G., Bogner S., Bührig-Polaczek A. Tensile creep of directionally solidified NiAl—9Mo in situ composites. Acta Mater. 2013. Vol. 61. P. 7155—7165. DOI: 10.1016/j.actamat.2013.08.017.
- 3. Seemüller C., Heilmaier M., Haenschke T., Bei H., Dlouhy A., George E.P. Influence of fiber alignment on creep in directionally solidified NiAl—10Mo in-situ composites. *Intermetallics*. 2013. Vol. 35. P. 110—115. DOI: 10.1016/j. intermet.2012.12.007.
- Bei H., George E.P. Microstructures and mechanical properties of a directionally solidified NiAl—Mo eutectic alloy. Acta Mater. 2005. Vol. 53. P. 69—77. DOI: 10.1016/j. actamat.2004.09.003
- Shang Z., Shen J., Wang L., Du Y., Xiong Y., Fu H. Investigations on the microstructure and room temperature fracture toughness of directionally solidified Ni-Al—Cr(Mo) eutectic alloy. *Intermetallics*. 2015. Vol. 57. P. 25—33. DOI: 10.1016/j.intermet.2014.09.012.
- 6. Walter J.L., Cline H.E. The effect of solidification rate on structure and high-temperature strength of the eutectic NiAl—Cr. Metal. Mater. Trans. B. 1970. Vol. 1. P. 1221—1229. DOI: 10.1007/bf02900234.
- Cui C.Y., Chen Y.X., Guo J.T., Li D.X., Ye H.Q. Preliminary investigation of directionally solidified NiAl—28Cr—5.5Mo—0.5Hf composite. Mater. Lett. 2000. Vol. 43. P. 303—308. DOI: 10.1016/S0167-577X(99)00278-5.
- 8. Войтович Р.Ф., Головко Э.И. Высокотемпературное окисление металлов и сплавов. Киев: Наукова думка, 1980.

  Voitovich R.F., Golovko E.I. High temperature oxidation of metals and alloys. Kiev: Naukova dumka, 1980.
- 9. *Klumpes R., Maree C.H.M., Schramm E., de Wit J.H.W.*The influence of chromiumon the oxidation of β-NiAl at 1000 °C. *Mater. Corros.* 1996. Vol. 47. P. 619—624.
- Johnson D.R., Chen X.F., Oliver B.F. Processing and mechanical properties of in-situ composites from the NiAlCr and the NiAl(Cr,Mo) eutectic systems. *Intermetallics*. 1995. Vol. 3. P. 99—113. DOI: 10.1016/0966-9795(95)92674-O.
- 11. Yang J.C., Schumann E., Levin I., Rühle M. Transient oxidation of NiAl. Acta Mater. 1998. Vol. 46. P. 2195—2201.
- 12. *Grabke H.* Oxidation of NiAl and FeAl. *Intermetallics*. 1999. Vol. 7. No. 10. P. 1153—1158. DOI: 10.1016/S0966-9795(99)00037-0.

- Gao W., Li Z., Wu Z., Li S., He Y. Oxidation behavior of Ni<sub>3</sub>Al and FeAl intermetallics under low oxygen partial pressures. *Intermetallics*. 2002. Vol. 10. No. 3. P. 263—270. DOI:10.1016/S0966-9795(01)00132-7.
- Bo L., Fei L., Cong L., Yimin G., Congmin F., Xiaohu H.
   Effect of Cr element on the microstructure and oxidation resistance of novel NiAl-based high temperature lubricating composites. Corrosion Sci. 2021. Vol. 188. Art. 109554.

   DOI: 10.1016/j.corsci.2021.109554.
- Geramifard G., Gombola C., Franke P., Seifert H.J. Oxidation behaviour of NiAl intermetallics with embedded Cr and Mo. Corrosion Sci. 2020. Vol. 177. Art. 108956. DOI: 10.1016/j.corsci.2020.108956.
- Hea Y., Luo L., Sushko M., Liu C, Baer D., Schreiber D., Rosso K., Wang Ch. Vacancy ordering during selective oxidation of β-NiAl. Materialia. 2020. Vol. 12. Art. 100783. DOI: 10.1016/j.mtla.2020.100783.
- Санин В.В., Филонов М.Р., Юхвид В.И., Аникин Ю.А., Михайлов А.М. Исследование влияния температуры переплава на структурную наследственность сплавов, полученных методом центробежной СВС-металлургии. Известия вузов. Цветная металлургия. 2016. No. 1. C. 63—71. DOI: 10.17073/0021-3438- 2016-1-63-71.
  - Sanin V.V., Filonov M.R., Yukhvid V.I., Anikin Y.A., Mikhailov A.M. Investigation into the influence of the remelting temperature on the structural heredity of alloys fabricated by centrifugal SHS metallurgy. Russ. J. Non-Ferr. Met. 2016. Vol. 57. No. 2. P. 124—130. DOI: 10.3103/S1067821216020097.
- Zaitsev A.A., Sentyurina Zh.A., Levashov E.A., Pogozhev Yu.S., Sanin V.N., Loginov P.A., Petrzhik M.I. Structure and properties of NiAl—Cr(Co,Hf) alloys prepared by centrifugal SHS casting. Part 1 — Room temperature investigations. Mater. Sci. Eng. A. 2017. Vol. 690 P. 463—472. DOI: 10.1016/j.msea.2016.09.075.
- Zaitsev A.A., Sentyurina Zh.A., Levashov E.A., Pogozhev Yu.S., Sanin V.N., Sidorenko D.A. Structure and properties of NiAl—Cr(Co,Hf) alloys prepared by centrifugal SHS casting followed by vacuum induction remelting. Part 2 Evolution of the structure and mechanical behavior at high temperature. Mater. Sci. Eng. A. 2017. Vol. 690. P. 473—481. DOI: 10.1016/j.msea. 2017.02.089.
- 20. Kaplanskii Yu.Yu., Zaitsev A.A., Levashov E.A., Pogozhev Yu.S., Loginov P.A., Sentyurina Zh.A., Logacheva A.I. The structure and properties of pre-alloyed NiAl—

- Cr(Co,Hf) spherical powders produced by plasma rotating electrode processing for additive manufacturing. *J. Mater. Res. Technol.* 2018. Vol. 7. No. 4. P. 461—468. DOI: 10.1016/j.jmrt.2018.01.003.
- Kaplanskii Yu.Yu., Zaitsev A.A., Levashov E.A., Loginov P.A., Sentyurina Zh.A. NiAl based alloy produced by HIP and SLM of pre-alloyed spherical powders. Evolution of the structure and mechanical behavior at high temperatures. *Mater. Sci. Eng. A.* 2018. Vol. 717. P. 48—59. DOI: 10.1016/j.msea.2018.01.057.
- Kurbatkina V.V. Nickel aluminides. In: Concise Encycl. Self-Propagating High-Temperature Synth. Elsevier, 2017. P. 212—213. DOI: 10.1016/B978-0-12-804173-4.00099-5.
- Kurbatkina V.V., Patsera E.I., Levashov E.A., Kaplanskii Y.Y., Samokhin A.V. Fabrication of narrow-fraction micropowders of nial-based refractory alloy compoNiAl—M5-3. Int. J. SHS. 2018. Vol. 27. P. 236—244. DOI: 10.3103/S1061386218040027.
- Tsvetkov Yu.V., Samokhin A.V., Alekseev N.V., Fadeev A.A., Sinaiskii M.A., Levashov E.A., Kaplanskii Yu.Yu. Plasma spheroidization of micropowders of a heat-resistant alloy based on nickel monoaluminide. *Doklady Chemistry*. 2018. Vol. 483. Pt. 2. P. 312—317. DOI: 10.1134/ S0012500818120030.
- 25. Kaplansky Yu.Yu., Levashov E.A., Korotitskiy A.V., Loginov P.A., Sentyurina Zh.A., Mazalov A.B. Influence of

- aging and HIP treatment on the structure and properties of NiAl-based turbine blades manufactured by laser powder bed fusion. *Additive Manufacturing*. 2020. Vol. 31. Art. 100999. DOI: 10.1016/j.addma.2019.100999.
- Sanin V.V., Kaplansky Y.Y., Aheiev M.I., Levashov E.A., Petrzhik M.I., Bychkova M.Y., Samokhin A.V., Fadeev A.A., Sanin V.N. Structure and properties of heat-resistant alloys NiAl—Cr—Co—X (X = La, Mo, Zr, Ta, Re) and fabrication of powders for additive manufacturing. Materials. 2021. Vol. 14. No. 12. Art. 3144. DOI: 10.3390/ma14123144.
- Kaplanskii Y.Y., Levashov E.A., Bashkirov E.A., Korotits-kiy A.V. Effect of molybdenum on structural evolution and thermomechanical behavior of a heat-resistant nickel aluminide-based alloy. J. Alloys Compd. 2022, Vol. 892. Art. 162247. DOI: 10.1016/j.jallcom.2021.162247.
- 28. Baskov F.A., Sentyurina Zh.A., Kaplanskii Yu.Yu., Logachev I.A., Semerich A.S., Levashov E.A. The influence of post heat treatments on the evolution of microstructure and mechanical properties of EP741NP nickel alloy produced by laser powder bed fusion. Mater. Sci. Eng. A. 2021. Vol. 817. Art. 141340. DOI: 10.1016/j.msea.2021.141340.
- Zhang W.L., Li S.M., Fu L.B., Li W., Sun J., Wang T.G., Jiang S.M., Gong J., Sun C. Preparation and cyclic oxidation resistance of Hf-doped NiAl coating. Corrosion Sci. 2022. Vol. 195. Art. 110014. DOI: 10.1016/j.corsci. 2021.110014.